12

Specialized detectors

The detectors discussed to this point, scintillation counters, Cerenkov counters, proportional chambers, and drift chambers, can be found in some combination in most particle physics experiments. There are in addition other types of detectors that are used for specialized applications. These include such old standards as emulsions and bubble chambers, as well as the more recently developed transition radiation detectors and semiconductor detectors. This chapter contains a short discussion on some of the more common types of specialized detectors.

12.1 Bubble chambers

The bubble chamber was one of the most important detectors for particle physics experiments during the 1960s and early 1970s. Much of our knowledge of particle spectroscopy, strong interactions, and neutrino physics was learned with this device.

The detector consists of a cryogenic fluid, an expansion system, and usually a magnetic field. The expansion system, which typically involves a piston and bellows arrangement, is used to suddenly reduce the pressure on the chamber liquid. The liquid is initially maintained at a pressure above the equilibrium vapor pressure curve. Following a sufficiently rapid expansion, it is left in a "superheated" condition, and bubbles will form around any nucleation centers in the liquid. A charged particle will produce delta rays in the liquid, and the delta rays in turn can produce large numbers of ion pairs in a small volume. The recombination of these ion pairs produce a heat spike, which is thought to be responsible for bubble formation [1, 2].

When used in a particle physics experiment, the chamber expansion is synchronized with the arrival of a beam of particles from the accelerator.

Any charged particle that is in the beam or that is created from interactions in the chamber liquid will leave a trail of ions in the liquid. Bubbles that form around the ions typically grow to a diameter of $\sim 10\ \mu$m in 0.2 – 50 ms. At this point flash lights illuminate the chamber, and two or more cameras simultaneously take a picture of the tracks of bubbles. A magnetic field surrounding the chamber allows the particle momenta to be measured from the curvature of the tracks. After the pictures are taken, the expansion system recompresses the liquid and collapses the bubbles. The bubble density gives a measure of the ionization energy loss and can be used to determine the mass of particles with $\beta \leqslant 0.8$.

The chamber fluid can be liquid hydrogen, liquid deuterium, or a heavy liquid mixture. Liquid hydrogen provides free protons. Tracks measured in liquid hydrogen have relatively small errors due to multiple scattering. Liquid deuterium is used to extract information about interactions on quasi-free neutrons. Heavy liquids are useful for studying interactions involving photons, electrons, or neutrinos. The greater density provides more interactions per unit volume, while the higher Z gives shorter γ ray conversion lengths. The virtues of liquid hydrogen and the heavy liquid can be combined by filling a track sensitive target with liquid hydrogen and locating it inside the volume of a heavy liquid chamber.

Bubble chambers offer a number of advantages. They have 4π acceptance, excellent tracking efficiency, good spatial resolution, mass identification for slow particles, and efficient observation of secondary decay vertices. On the other hand, several disadvantages led to a decline in the use of the method. The standard chamber cannot be triggered. Thus, many pictures are taken that do not contain useful information. Analysis of the film is a lengthy process that may take several years. Bubble chambers cannot efficiently use a high beam rate. Moderate sized chambers cannot make an accurate measurement of high momentum tracks, and they cannot be used at colliding beam machines.

Some of these difficulties may be overcome with the use of hybrid bubble chamber systems [3]. These systems involve using the bubble chamber in conjunction with counters or wire chambers. Modern neutrino experiments often use a large volume bubble chamber together with an external muon identifier. The rapid cycling bubble chamber at SLAC can cycle 20 – 100 times faster than standard chambers, making it suited to the fast repetition rate of the SLAC accelerator. The hybrid system includes wire chambers for accurate measurement of high momentum particles and a Cerenkov counter to aid in particle identification. The system may be operated in a triggered mode and is very effective in studying processes with a fast forward particle.

Benichou et al. [4] have constructed a small special purpose bubble chamber (LEBC) to study the production of rare, short-lived particles. The chamber was machined from Lexan plastic and had a volume of only 1.1 liters. Because the cross section for the production of the particles was small, the chamber was designed to cycle with a 33-Hz repetition rate. High resolution was necessary to clearly separate the particle production and decay vertices.

Figure 12.1 shows the pressure–temperature characteristics of low temperature hydrogen. The equilibrium vapor pressure is shown together with the foam limit. Pressure–temperature points below the foam limit curve are subject to free bubble formation. The vertical lines indicate the

Figure 12.1 The pressure–temperature characteristics of low temperature hydrogen. (J. Benichou et al., Nuc. Instr. Meth. 190: 487, 1981.)

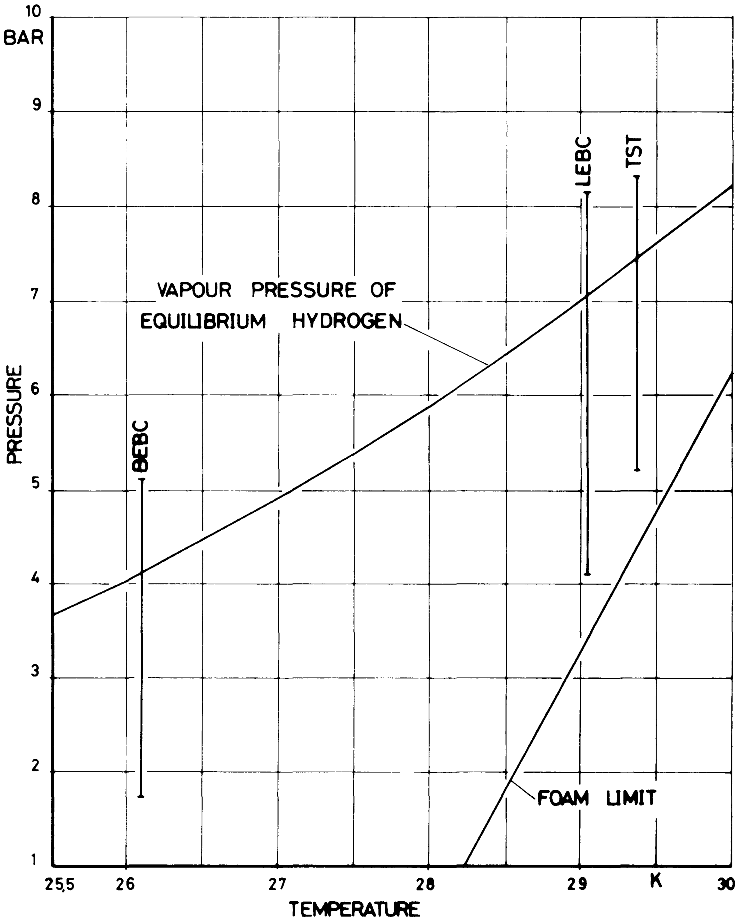

pressure range used in three bubble chambers. Normal chambers such as the Big European Bubble Chamber (BEBC) operate at lower temperatures than LEBC. The higher temperature allows LEBC to use a higher minimum pressure, resulting in slower bubble growth rate and better resolution [4].

Another possible improvement in bubble chamber technique involves the use of holography to replace the conventional photographic systems [5, 6]. This permits improvement of the optical resolution without losing depth of field and an increase in acceptable particle flux. In holography the film is illuminated with coherent light from a laser. Great care must be taken to prevent any thermal gradients or turbulence in the chamber liquid. The holographs must also be illuminated by laser on the scanning and measuring machines. Dykes et al. [5] used a pulsed ruby laser to make holograms with a spatial resolution of ~ 8 μm and with particle fluxes up to 150 particles per picture.

12.2 Emulsions

The detection of radiation by the exposure of photographic plates dates back to the discoveries of Röntgen and Bequerel. Emulsions are still used in experiments requiring the best possible spatial resolution.

The emulsion consists of three basic components: a silver halide, a gelatin-plasticizer, and water [7]. A layer of the emulsion, typically 600 μm thick, covers a plate, a number of which may be stacked together into a sandwich. Sometimes the emulsion is "loaded" with metal wires, foil, or powdered layers to give a well-defined target.

The halide grains have a diameter of ~ 0.2 μm. Ionization energy from a charged particle traversing the emulsion may cause the grain to develop. The production of delta rays with energy between 150 and 5000 eV plays an important role in developing the grains, since they are capable of providing a large energy deposit in a region similar in size to the grain volume. A minimum ionizing particle produces ~ 270 developed grains per millimeter of track length.

For stopping particles a measurement of the particle's range can be used to determine its energy. A measurement of the energy can also be derived from the density of delta rays. A measurement of the exposed grain density or the distribution of gaps between exposed grains can be used to measure the specific ionization or dE/dx of the track. At low energy this is proportional to $1/v^2$. Grain counts can be calibrated by measuring the distinctive electron tracks in nearby regions of the emulsion.

Grain density provides a means of particle identification for $\beta \leqslant 0.9$ but saturates for higher velocities. For relativistic particles measurements of the projected angles between successive chords on the track and the multiple scattering theory provide a determination of $p\beta$.

Events in the emulsion must be located in a tedious search using a microscope. Recent experiments [8] have used the emulsion in conjunction with a particle spectrometer. Long-lived tracks can be measured in the spectrometer and used to predict the position of the interaction vertex. This greatly reduces the volume of emulsion that must be examined.

12.3 Spark chambers

Spark chambers were used routinely during the period 1960–1975 for particle tracking measurements. They have since been almost totally replaced by MWPCs and drift chambers. One possible advantage for using spark chambers today is a smaller cost for the readout system for a large area detector.

The basic elements of a spark chamber are shown in Fig. 12.2. The chamber consists of metallic plates or wire grids separated by insulating

Figure 12.2 Principles of spark chamber operation. (S) Scintillation counter, (Co) coincidence circuit, (A) amplifier, and (sg) spark gap.

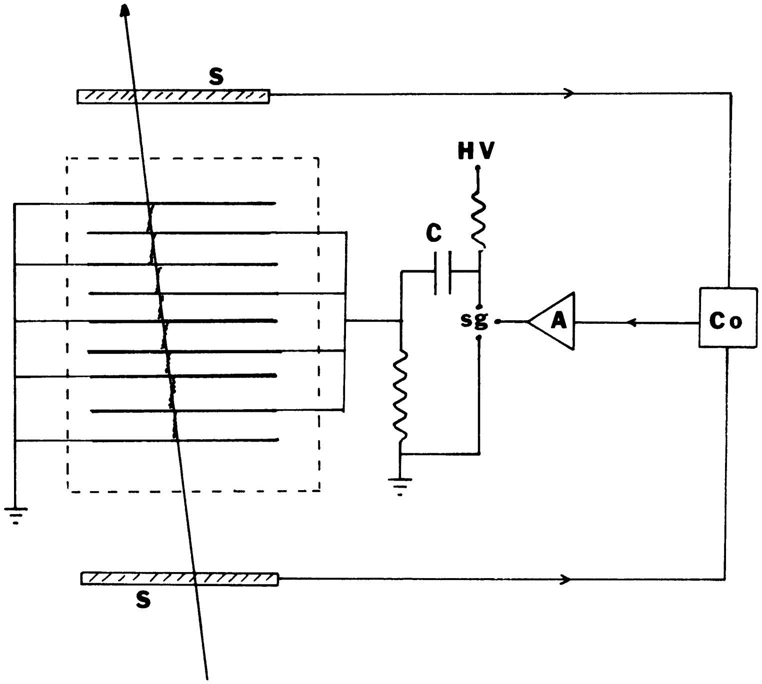

gaps and filled with a gas. A charged particle traversing the detector leaves a trail of ions in the gas. Usually a pair of scintillation counters or other fast responding devices are used in conjunction with the spark chamber. A coincidence signal from the two scintillators indicates the passage of a charged particle. The coincidence signal is amplified and applied to a spark gap or a thyratron. This produces a fast rising high voltage pulse. One plate of the capacitor C discharges quickly to ground. The charge on the opposite plate raises alternate plates of the detector to high voltage. The large potential difference causes a spark to form along the path of the ions in the gap. The locations of the sparks indicate the path of the particle. In a narrow gap chamber the sparks form at right angles to the electrodes, while in wide gap chambers the sparks tend to follow the actual path of the particle. The ions are cleared from the gap by maintaining a low voltage dc clearing field across the gap.

Spark formation requires a buildup of at least 10^8 electrons [9]. This leads to the Raether criterion: for a given chamber the applied field must be such that

$$d > 20/\alpha \tag{12.1}$$

where d is the gap separation and α is the Townsend coefficient. The formation time for the spark then is

$$\tau = 20/(\alpha w^-) \tag{12.2}$$

where w^- is the electron drift velocity. The high voltage pulse must remain on the electrodes for at least this period of time.

Important characteristics of spark chamber gases include α, the drift velocity, electron affinity, photoabsorption, specific ionization, diffusion coefficient, emission spectrum, and cost. The usual spark chamber gas is a mixture of neon and helium. Noble gases have zero electron affinity. Thus, electrons do not attach to the gas atoms, and substantial electron multiplications can occur. Small amounts of additional gases are sometimes added. Electronegative gases (e.g., Freon) help clear the chamber of residual ions. Some organic molecules (e.g., alcohol) are efficient absorbers of photons. The addition of such a gas prevents a photon from liberating an electron some distance from the site of ionization and initiating spurious sparks.

The operation of the spark chamber pulsing system is of the utmost importance. The pulse should be applied as rapidly as possible to minimize diffusion and unrelated sparks and to ensure optimum spark formation. There must be sufficient energy to allow many sparks to form simultaneously. The system must have a short recovery time so that the chamber can be used in moderately high rate environments.

The high voltage switch is a thyratron tube or spark gap. Thyratrons are capable of producing 1000-A pulses in 15–30 ns. This high voltage is applied to the chamber as symmetrically as possible using coaxial cable or insulated stripline. The chamber itself behaves like a waveguide, leading to reflections at the edges unless the electrodes are properly terminated.

Referring to Fig. 12.2, the voltage applied to the spark gap is

$$V_{\text{gap}} = CV/(C + C_{\text{sc}}) \tag{12.3}$$

where C_{sc} is the capacitance of the chamber itself. A large 1-m^2 chamber may have a capacitance $C_{\text{sc}} \sim 1000$ pF. A proper treatment of the chamber's electrical properties should include the inductances of the leads, which are important when considering very fast pulses [9].

In the absence of a magnetic field the ions are displaced across the spark chamber gap because of the clearing field. The displacement is $w\,\Delta t_1$, where w is the drift velocity and Δt_1 is the time from the creation of the ion until the high voltage (HV) pulse is applied. During the initial risetime of the HV pulse the ions undergo an additional drift of $w\,\Delta t_2$. The clearing field and high voltage pulse are ordinarily adjusted with opposite polarity so that these displacements tend to cancel. The effect leads to an angle dependent correction to the measured track position

$$\Delta x = b + m \tan\theta \tag{12.4}$$

In addition, it is sometimes desirable to alternate the direction of the clearing field in alternate gaps.

Spark chambers can routinely achieve 95% efficiency for the detection of a single charged particle. The efficiency is a function of the static clearing field and the time delay before pulsing the chamber. For a given clearing field, if one waits too long before applying the HV pulse, all the ions will be cleared from the gap and no spark will form. Multispark efficiency is enhanced with wide gaps and fast HV risetimes [9].

The spatial resolution of a wire plane spark chamber is roughly $\pm s/2$, where s is the wire spacing. This can be improved to $\pm s/4$ by adjusting the pulse so that several wires participate in the discharge [9]. Typical spatial resolutions are ± 300 μm. The resolution is influenced by a number of factors. Since the ions are typically produced with several electron volts of kinetic energy, they can diffuse before the application of the HV pulse. The spark channel itself may have a width of ~ 1 mm [9]. For narrow gap chambers the spark discharge is perpendicular to the electrodes and forms near the cathode, even for inclined tracks. The spatial accuracy is improved at higher gas pressures.

The time resolution, or "memory time," of the chamber must be long enough so that ions are still in the gap when the logic system determines if the event is of interest, yet short enough so that the gaps are not full of ions from unwanted events. This time is determined by the value of the clearing field and the HV pulse delay and by the addition of electronegative gases. A typical memory time is 1 μs, enabling the chamber to be used in a beam flux of 10^6 particles/sec. Following a HV pulse, the chamber requires a recovery (dead) time of ~ 1 ms to clear the gap of debris. The electrons clear from the gap first, leaving the slower positive ions and meta-stable atoms.

The occurrence of a spark leads to a number of optical, electrical, and acoustic phenomena that can be used to determine the position of the spark. A list of some readout methods and the physical principles they rely on are given in Table 12.1. We will describe the magnetostrictive readout method. For a discussion of other methods the reader is referred elsewhere [9, 10].

Table 12.1. *Spark chamber detection systems*

Method	Principle
1. Optical	picture of spark recorded on film
2. Vidicon	optical image transformed into electrical signal by TV camera
3. Sonic	propagation time in gas used to localize spark
4. Ferrite core	current flowing in wire electrode sets ferrite memory core
5. Magnetostriction	magnetic field of spark induces acoustic wave in magnetostrictive wire
6. Delay line	propagation time of signals induced by sparks in electrode or in external delay line separating wires permits localization of spark
7. Current division	amount of charge carried in spark split between two channels; difference in charge measured on transformer filter circuit gives position
8. Sparkostriction	auxiliary spark produced against a wire at small distance from electrode; time of propagation in this nonmagnetic wire gives position of spark
9. Capacitive	current in each wire charges capacitor that can subsequently be read out
10. Spark projection	low frequency potentials of wire chamber transported by external wires to second plane; auxiliary spark produced and viewed by vidicon tube
11. Magnetic tape	sparks produce signal on magnetic tape used as electrode

Source: G. Charpak, Ann. Rev. Nuc. Sci. 20: 195, 1970.

Magnetostriction is a property of certain ferromagnetic materials whereby a magnetic field induces a stress in the material. Magnetostrictive wires are placed across the leads of the spark chamber electrodes [11]. The current from the spark creates a magnetic field around the wire. The field changes the magnetization in the magnetostrictive wire and creates an acoustic pulse in the wire. The pulse has both longitudinal and torsional modes. The longitudinal mode is dispersive, but its detection is simpler. Acoustic pulses travel in both directions with velocity $\sqrt{E/\rho}$, where E is the elastic modulus and ρ is the density. For iron–cobalt wire, $v \sim 5$ mm/μs. At each end of the magnetostrictive wire is a pickup coil. Here the acoustic wire induces a current by the inverse, or Villari, effect. The arrival times of the pulses at the two detectors can be used to determine the position of the spark. Multiple sparks can be detected by counting oscillator pulses in sets of scalers, which have been simultaneously started at the arrival of the first fiducial, and stopped one by one as signals from the sparks are received from the magnetostrictive pickup coils.

Magnetostrictive readout is difficult to use in a magnetic field because the field affects the shape of the magnetostrictive pulse. This necessitates bringing the spark chamber wires outside the region of the field before being read out. For operation inside a field it is often simpler to use some other method, such as capacitive readout.

12.4 Streamer chambers

The streamer chamber is in some respects an electronic analog of the bubble chamber. Charged particles passing through the chamber gas leave the usual trail of ionization. The chamber volume is subjected to an electric field of 10–50 kV/cm for a short period of 5–20 ns. Electron avalanches develop into expanding, conducting plasmas known as streamers when their space charge field is comparable to the applied field. The streamers move at high velocity toward both electrodes. At the end of the high voltage pulse the streamers remain suspended in the chamber [9]. The ions recombine and emit light, which reveals their location and thus the particle trajectories. Some virtues of the streamer chamber are that many tracks may be followed over large distances, it has isotropic response, and unlike the bubble chamber, it can be triggered. One disadvantage is the lower density.

The basic elements of a streamer chamber are similar to the spark chamber. A coincidence signal from scintillation counters indicate the passage of a particle. A large high voltage pulse is created with a Marx generator. This consists of a set of capacitors that are charged up slowly in parallel and discharged rapidly in series. The high voltage pulse must be very short to stop the spark development at the streamer stage. Thus, a shaping network is necessary before the pulse is applied to the electrodes. Sharp pulses 20 ns in duration are typical.

The appearance of the streamer depends on the relative orientation of the camera, the electrodes, and the particle trajectory. A typical streamer chamber gas is 90% neon and 10% helium. The memory time is controlled by the addition of electronegative gases such as SF_6.

The chamber is practically 100% efficient for single tracks, since many ions are liberated along the particle trajectory. Multitrack efficiencies are also very high. The chamber can operate in a high rate environment. Some particle identification is possible below 1 GeV/c by using the streamer density.

The streamers are created with a width of about 1 mm. Particle trajectories can be located with an accuracy of about 300 μm. The resolution improves as the gas pressure is increased because the avalanche reaches the same total ionization in a smaller distance. Two effects that lead to systematic errors in locating the track are the drift of the ionization electrons during the rise of the high voltage pulse and the fact that streamers develop symmetrically about the head of the avalanche and not about the site of the original ionization. A high pressure streamer chamber constructed at Yale University [12, 13] is capable of measuring track positions with a spatial resolution of 40 μm.

12.5 Transition radiation detectors

Devices utilizing transition radiation have proven useful for the detection of electrons and show promise for providing particle identification at high energies. An important feature of such radiation is that its intensity can be made to increase linearly with the Lorentz factor γ.

A charged particle emits transition radiation when it crosses the interface between media with different dielectric or magnetic properties. When the particle is in the region of low dielectric constant, polarization effects in the surrounding medium are small, and the electric field associated with the moving charge has a large spatial extent. However, when the particle crosses the interface to a region of higher dielectric constant, polarization effects are larger, thereby reducing the extent of the electric field in the medium. The sudden redistribution of charges in the medium associated with the changing electric field of the particle gives rise to the transition radiation.

At high energy transition radiation is primarily emitted as X-rays. The total energy emitted upon crossing a single surface is [14]

$$W = \tfrac{2}{3}\,\alpha\omega_p\gamma \tag{12.5}$$

where α is the fine structure constant and ω_p is the plasma frequency of the medium,

$$\omega_p^2 = \frac{4\pi\alpha Z N_A \rho}{A m_e} \tag{12.6}$$

The mean number of X-rays emitted per surface is

$$\langle N\rangle \sim \tfrac{1}{2}\,\alpha \tag{12.7}$$

The X-rays are emitted strongly forward into a cone at an angle θ with respect to the particle direction given by

$$\theta \sim 1/\gamma \tag{12.8}$$

Practical detectors are made up of stacks of thin foils, thereby providing many interfaces. As soon as more than one surface is present, interference effects can arise from the superposition of the radiation. Foils must have a minimum thickness, known as the formation zone, so that the electromagnetic field of the particle can fully develop in the entered medium. The photon yield drops off sharply for foils thinner than the formation zone. The interference causes oscillations in the intensity as a function of ω, the photon frequency, and gives rise to γ thresholds where the intensity increases sharply.

A number of practical transition radiation detectors have been constructed. Cobb et al. [15] have built a carefully optimized transition detector for electron – hadron separation at the ISR. The device consisted of two groups of ~ 700 foil radiators followed by a MWPC detector. The foil spacing was chosen to provide constructive interference. The radiators had to have a small X-ray absorption so that the photons could reach the detector. This and other requirements lead to the choice of thin 53-μm lithium metal foils as the radiator. The threshold parameter γ_t for the device is proportional to the foil thickness d,

$$\gamma_t = \frac{d\omega_{\mathrm{Li}}}{2c} \tag{12.9}$$

where ω_{Li} is the plasma frequency in lithium (14.2 eV/$\hbar$). One problem with a detector of this type is that the charged incident particle also passes through the MWPC and deposits ionization energy in the chamber gas. A xenon – CO_2 mixture was found to efficiently detect the transition X-rays and to give the best ratio of X-ray absorption to charged particle ionization. The detector was able to count electrons with good efficiency and with a substantial rejection for hadrons.

If a large distance is available between the radiator and detector, it is possible to improve the particle discrimination by using information about the width of the pulse. Deutschmann et al. [16] analyzed the current signals from a drift chamber using 16 analog to digital converters triggered by 16 successive 30-ns gates. Electrons with $p = 15$ GeV/c showed a considerably wider distribution than 15-GeV/c pions due to the presence of transition radiation in the electron sample.

It is also possible to improve the detector's sensitivity by counting the number of charge clusters along the particle's track in a drift chamber. Ludlam et al. [17] and Fabjan et al. [18] measured the deposited charge in 20-ns intervals of drift time. They defined a cluster to be the amount of charge deposited in any 100-ns interval corresponding to an energy of 2 keV. The 100-ns time interval was equivalent to a spatial extent of 850 μm. The number of clusters is expected to follow a Poisson distribution. Figure 12.3 shows the experimental data for the number of clusters versus γ. It can be seen that the presence of lithium radiators leads to a greater number of clusters due to interactions of the transition radiation photons in the drift chamber gas.

12.6 Short summary of some other detectors

12.6.1 Semiconductor detectors

Semiconductor counters behave like solid ionization chambers [19, 20]. Incident charged particles deposit ionization energy and dislodge electrons, which in turn produce secondary ionization. This causes a separation of the electrons and holes in the semiconductor, which then separate due to the presence of an electric field. They collect at the electrodes, giving a signal proportional to the deposited energy. The detector has better resolution than gaseous ion chambers since the average energy required to produce an ion pair in silicon is 3.6 eV, for instance, while it is typically ~30 eV in gases. Semiconductor detectors are useful when a thin, high resolution detector is required near an interaction region. Silicon surface barrier detectors have high efficiency and high rate capability and can operate inside a colliding beam vacuum chamber. The principle disadvantages are small size and radiation damage.

Amendolia et al. [21] used a stack of silicon surface barrier detectors as an active target. They identified the layer where the interaction occurred from the large pulse height resulting from the recoil nucleus. The pulse height from the subsequent layers gave information on the particle multiplicity as a function of the distance from the interaction point.

A slice of silicon can also be etched to give narrow strips of active detector [20, 22]. This provides a small area device that behaves like a MWPC but has better spatial resolution, especially for multitrack events. Such a detector is shown in Fig. 12.4. A relativistic, singly charged particle produces about 25,000 electron-hole pairs while crossing this detector [22]. All the charge is collected within 10 ns. A telescope consisting of six

Figure 12.3 Number of ionization clusters in a drift chamber as a function of the relativistic γ factor. The upper curve shows the data with lithium radiator foils. (After T. Ludlam et al., Nuc. Instr. Meth. 180: 413, 1981.)

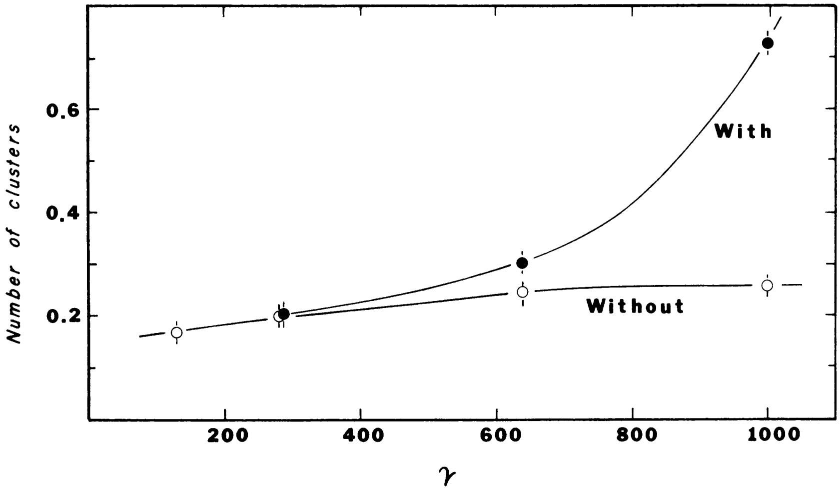

Figure 12.4 Cross section of a silicon microstrip detector. (B. Hyams et al., Nuc. Instr. Meth. 205: 99, 1983.)

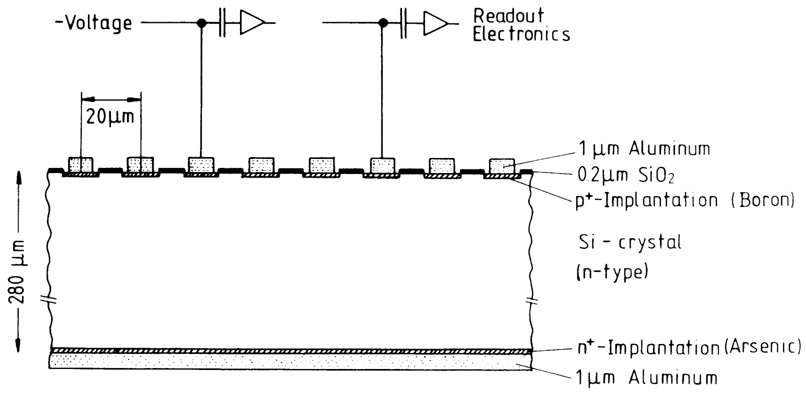

of these silicon microstrip detectors has achieved 5 μm spatial resolution for minimum ionizing particles.

12.6.2 Flashtube hodoscope chambers

The flashtube chamber is similar in operation to a spark chamber [23]. The hodoscope is made up of many tubes containing neon gas. An external trigger sensitizes each tube by initiating the application of a high voltage pulse. If any ions are in a tube due to the passage of a charged particle, a streamer will form, and the tube emits a pulse of light. This is either detected directly or causes a transducer to generate an electrical pulse.

Large arrays of flashtubes have been used in calorimeters and for studying cosmic ray showers. The chief advantage of the device is the low cost to construct a large volume array. The spatial resolution is on the order of the tube diameter (~ 2 mm). The tube can be sensitive for ~ 1 μs and has ~ 10 ms recovery time, depending on the gas composition and clearing field used.

12.6.3 Stopping K^+ detector

Detectors have been constructed that can efficiently indicate the presence of a K^+ [24, 25]. Astbury et al. [24] have built a detector consisting of 17 alternating layers of brass and scintillator. The range–energy relations show that for particles with $p \leqslant 600$ MeV/c, μ and π^+ have a much greater range than K^+ and p. Thus, by using the proper amount of brass absorber, K^+ and p will stop in the detector. This is indicated by a large pulse height in the scintillator preceding the stopping layer and no signal in the following layer. The K^+ will then subsequently decay, while the proton will not. Thus, a K^+ should have in addition a small pulse height signal in a scintillator after a suitable delay period. The detector achieved a high efficiency for identifying K^+ with a good rejection for π^+. This method can also be applied to make a trigger for stopping muons.

12.6.4 Planar spark counters

Planar spark counters have been used in applications such as time of flight measurements where it is desirable to obtain the best possible timing resolution. One such device constructed for use at PEP consisted of two parallel electrodes separated by 185 μm with a field $\sim 2\ 10^5$ V/cm maintained across the gap [26]. The anode was constructed from semiconducting glass. A noble gas–organic quencher mixture flowed through the gap at high pressure. The signal from a discharge had a typical risetime of ~ 1 ns and a pulse length of about 5 ns. The counter recovered within a few milliseconds.

The PEP planar spark counters had timing resolutions better than 200 ps under actual experimental conditions [26]. The measured single counter time distribution for Bhabha scattering events are shown in Fig. 12.5, together with the time of flight distribution. The "albedo" events in the histogram are due to electrons and positrons scattered backward from a nearby shower counter. The albedo events occur later and have a

Figure 12.5 Single counter Bhabha scattering time distributions for two spark counters (T1, T2) and the resulting time of flight spectrum (TOF). The dotted curves are due to backward scattered (albedo) events. (After W. Atwood et al., Nuc. Instr. Meth. 206: 99, 1983.)

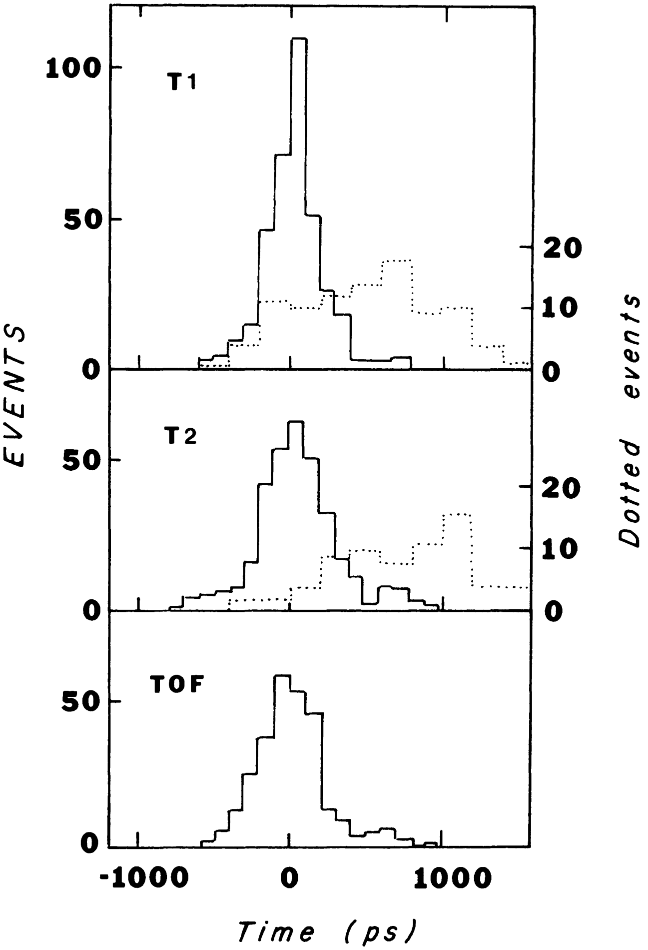

broader distribution than the incident Bhabha particles. The spatial resolution of the counter was 2.6 mm, consistent with the least count of the TDCs used to make the measurement. The pulse height was well correlated with the number of particles striking the counter. There was, however, a degradation in the pulse height and the timing resolution when the counting rate was ⩾300 Hz.

References

[1] R. Shutt (ed.) *Bubble and Spark Chambers,* New York: Academic, 1967.
[2] T. Dombeck and J. Vanhoy, A study of the bubble formation mechanism in a hydrogen bubble chamber using e^- and e^+ tracks, Nuc. Instr. Meth 177: 347-52, 1980.
[3] J. Ballam and R. Watt, Hybrid bubble chamber systems, Ann. Rev. Nuc. Sci. 27: 75-138, 1977.
[4] J. Benichou, A. Herve, H. Leutz, G. Passardi, W. Seidl, J. Tischhauser, H. Wenninger, and C. Fisher, A rapid cycling hydrogen bubble chamber with high spatial resolution for visualizing charmed particle decays, Nuc. Instr. Meth. 190: 487-502, 1981.
[5] M. Dykes, P. Lecoq, D. Gusewell, A. Herve, H. Wenninger, H. Royer, B. Hahn, E. Hugentobler, E. Ramseyer, and M. Boratav, Holographic photography of bubble chamber tracks: A feasibility test, Nuc. Instr. Meth. 179: 487-93, 1981.
[6] A. Herve, K. Johansson, P. Lecoq, P. Olivier, J. Pothier, L. Veillet, G. Waurick, and S. Tavernier, Performance of the holographic bubble chamber HOBC, Nuc. Instr. Meth. 202: 417-26, 1982.
[7] C. Powell, P. Fowler, and D. Perkins, *The Study of Elementary Particles by the Photographic Method,* New York: Pergamon, 1959.
[8] N. Ushida, T. Kondo, G. Fujioka, H. Fukushima, S. Tatsumi, Y. Takahashi, C. Yokoyama, Y. Homma, Y. Tsuzuki, S. Bahk, C. Kim, J. Park, J. Song, D. Bailey, S. Conetti, J. Fischer, J. Trischuk, H. Fuchi, K. Hoshino, M. Miyanishi, K. Niu, K. Niwa, H. Shibuya, Y. Yanagisawa, S. Errede, M. Gutzwiller, S. Kuramata, N.W. Reay, K. Reibel, T.A. Romanowski, R. Sidwell, N.R. Stanton, K. Moriyama, H. Shibata, T. Hara, O. Kusumoto, Y. Noguchi, M. Teranaka, H. Okabe, J. Yokota, J. Harnois, C. Hebert, J. Hebert, S. Lokanathan, B. McLeod, S. Tasaka, P. Davis, J. Martin, D. Pitman, J.D. Prentice, P. Sinervo, T.S. Yoon, H. Kimura, and Y. Maeda, Measurement of the D^0 lifetime, Phys. Rev. Lett. 45: 1049-52, 1980.
[9] P. Rice-Evans, *Spark, Streamer, Proportional, and Drift Chambers,* London: Richelieu, 1974, Chaps. 3-6.
[10] G. Charpak, Evolution of the automatic spark chambers, Ann. Rev. Nuc. Sci. 20: 195-254, 1970.
[11] K. Foley, W. Love, S. Ozaki, E. Platner, A. Saulys, E. Willen, and S. Lindenbaum, The Brookhaven double vee magnetic spectrometer, Nuc. Instr. Meth. 108: 33-60, 1973.
[12] J. Sandweiss, The high resolution streamer chamber, Phys. Today, Oct. 1978, pp. 40-45.
[13] R. Majka, T. Cardello, S. Dhawan, A. Disco, R. Kellog, T. Ludlam, P. Nemethy, J. Sandweiss, A. Slaughter, L. Tzeng, and I. Winters, Design and performance of a high resolution streamer chamber, Nuc. Instr. Meth. 192: 241-52, 1982.
[14] X. Artru, G. Yodh, and G. Mennessier, Practical theory of the multi-layered transition radiation detector, Phys, Rev. D 12: 1289-1306, 1975.
[15] J. Cobb, C. Fabjan, S. Iwata, C. Kourkoumelis, A. Lankford, G. Moneti, A. Nappi,

R. Palmer, P. Rehak, W. Struczinski, and W. Willis, Transition radiators for electron identification at the CERN ISR, Nuc. Instr. Meth. 140: 413–27, 1977.

[16] M. Deutschmann, W. Struczinski, C. Fabjan, W. Willis, I. Gavrilenko, S. Maiburov, A. Shmeleva, P. Vasiljev, V. Tchernyatin, B. Dolgoshein, V. Kantserov, P. Nevski, and A. Sumarokov, Particle identification using the angular distribution of transition radiation, Nuc. Instr. Meth. 180: 409–12, 1981.

[17] T. Ludlam, E. Platner, V. Polychronakos, M. Deutschmann, W. Struczinski, C. Fabjan, W. Willis, I. Gavrilenko, S. Maiburov, A. Shmeleva, P. Vasiljev, V. Chernyatin, B. Dolgoshein, V. Kantserov, P. Nevski, and A. Sumarokov, Particle identification by electron cluster detection of transition radiation photons, Nuc. Inst. Meth. 180: 413–18, 1981.

[18] C. Fabjan, W. Willis, I. Gavrilenko, S. Maiburov, A. Shmeleva, P. Vasiljev, V. Chernyatin, B. Dolgoshein, V. Kantserov, P. Nevski, and A. Sumarokov, Practical prototype of a cluster counting transition radiation detector, Nuc. Instr. Meth. 185: 119–24, 1981.

[19] G. Dearnalley and D. Northrop, *Semiconductor Counters for Nuclear Radiation*, London: Spon, 1963.

[20] R. Rancoita and A. Seidman, Silicon detectors in high energy physics: physics and applications, Rivista del Nuovo Cimento Vol. 5, No. 7, 1982.

[21] S.R. Amendolia, G. Batignani, E. Bertolucci, L. Bosisio, C. Bradaschia, M. Budinich, F. Fidecaro, L. Foa, E. Focardi, A. Giazotto, M.A. Giorgi, M. Givoletti, P.S. Marrocchesi, A. Menzione, D. Passuello, M. Quaglia, L. Ristori, L. Rolandi, P. Salvadori, A. Scribano, A. Stefanini, and M.L. Vincelli, Construction and performance of a silicon target for the decay path measurement of long lived mesons, Nuc. Instr. Meth. 176: 449–56, 1980.

[22] B. Hyams, U. Koetz, E. Belau, R. Klanner, G. Lutz, E. Neugebauer, A. Wylie, and J. Kemmer, A silicon counter telescope to study short lived particles in high energy hadronic interactions, Nuc. Instr. Meth. 205: 99–105, 1983.

[23] M. Conversi and G. Brosco, Flashtube hodoscope chambers, Ann. Rev. Nuc. Sci. 23: 75–122, 1973.

[24] J. Astbury, D. Binnie, A. Duane, J. Gallivan, J. Jafar, M. Letheren, J. McEwen, D. Miller, D. Owen, V. Steiner, and D. Websdale, A large detector for slow K^+ mesons, Nuc. Instr. Meth. 115: 435–43, 1974.

[25] C. M. Jenkins, J. Albright, R. Diamond, H. Fenker, J.H. Goldman, S. Hagopian, V. Hagopian, W. Morris, L. Kirsch, R. Poster, P. Schmidt, S.U. Chung, R. Fernow, H. Kirk, S. Protopopescu, D. Weygand, B. Meadows, Z. Bar-Yam, J. Dowd, W. Kern, and M. Winik, Existence of Ξ resonances above 2 GeV, Phys. Rev. Lett. 51: 951–4, 1983.

[26] W. Atwood, G. Bowden, G. Bonneaud, D. Klem, A. Ogawa, Y. Pestov, R. Pitthan, and R. Sugahara, A test of planar spark counters at the PEP storage ring, Nuc. Inst. Meth. 206: 99–106, 1983.

Exercises

1. A 10-GeV/*c* pion beam produces 10 bubbles/cm in a liquid hydrogen bubble chamber. What is the maximum energy required for bubble formation? How does this compare with the energy required to develop a grain in an emulsion?

2. What field is necessary for spark formation in a neon spark chamber with a 1-cm gap?

3. What clearing field is necessary to remove all the electrons from the 1-cm gap of a neon spark chamber within 1 μs?

4. Find the total energy lost to transition radiation by a 100-GeV/c proton traversing 500 lithium foils. Ignore interference effects. What is the mean number of emitted X-rays?